

Journal of  
**Applied Remote Sensing**

**Neural network cloud screening  
algorithm Part II: global synthetic  
cases using high resolution spectra in  
O<sub>2</sub> and CO<sub>2</sub> near infrared absorption  
bands in nadir and sun glint**

Thomas E. Taylor  
D. M. O'Brien

# Neural network cloud screening algorithm

## Part II: global synthetic cases using high resolution spectra in O<sub>2</sub> and CO<sub>2</sub> near infrared absorption bands in nadir and sun glint

Thomas E. Taylor,<sup>a</sup> and D. M. O'Brien<sup>b</sup>

<sup>a</sup>Department of Atmospheric Science, Colorado State University, Fort Collins, CO 80523  
[tommy@atmos.colostate.edu](mailto:tommy@atmos.colostate.edu)

<sup>b</sup>Cooperative Institute for Research in the Atmosphere, Fort Collins, CO 80523  
[obrien@atmos.colostate.edu](mailto:obrien@atmos.colostate.edu)

**Abstract.** In Part I a set of two layer feed-forward neural networks, trained via back propagation of sensitivities, was applied to a synthetic set of radiances in micro-windows of the near-infrared to make predictions of cloud water ( $c_w$ ), cloud ice ( $c_i$ ), effective scattering heights of cloud water and ice, ( $p_{cw}$  and  $p_{ci}$ , respectively) and the column water vapor ( $w$ ). A threshold test, using  $2 \text{ gm}^{-2}$  for cloud water and  $10 \text{ gm}^{-2}$  for cloud ice, was applied to the retrieved values to distinguish clear from cloudy scenes.

In that work the discussion was limited to the nadir viewing geometry, and was applied only to land surfaces, excluding desert and snow and ice fields. Part II describes the extension to a set of high resolution radiances, as might be measured by a grating spectrometer from space, in both nadir and sun glint viewing geometries. Furthermore, results are given for all land surface types as well as scenes over ocean.

Prior to neural network training, a Principal Component Analysis (PCA) is applied to the high resolution spectra, which consist of three bands centered at  $0.76 \mu\text{m}$  (O<sub>2</sub> A-band),  $1.61 \mu\text{m}$  (weak CO<sub>2</sub> band) and  $2.06 \mu\text{m}$  (strong CO<sub>2</sub> band), each with 1016 channels. Analysis shows that the five leading EOFs together capture 99.9% of the variance in each band, reducing the data size by more than two orders of magnitude. Application of the trained neural networks to an independent data set, generated using CloudSat and Calipso cloud and aerosol profiles, as well as carbon dioxide profiles from a chemical transport model, were used to quantify the skill in the retrieval. The results vary significantly with surface type, viewing mode and cloud properties. Accuracies range from 7% to 100% (typically close to 75%), with confidence levels almost always greater than 90%.

**Keywords:** neural networks, clouds, remote sensing, carbon dioxide, radiative transfer, satellites.

## 1 INTRODUCTION

This paper is the continuation of the work presented in the companion article [1] (hereafter referred to as Part I), which introduced a system of neural networks for estimating cloud amounts in the near-infrared spectral region. Information relevant to cloud is primarily contained in the depths of the absorption lines (O<sub>2</sub> and CO<sub>2</sub>); generally the lines are filled in when cloud is present. In Part I the subtleties associated with identifying clouds due to ambiguities in the spectra, especially in the O<sub>2</sub> A-band, were discussed.

The work presented here explores the application of the cloud retrieval to a set of synthetic radiances in the same three wavebands (O<sub>2</sub> A-band, weak CO<sub>2</sub> band and strong CO<sub>2</sub> band), but covering expanded spectral ranges with lower resolution than that used before. Note however,

that although the resolution used in this work is roughly an order of magnitude lower than that used in Part I (approximately  $0.3 \text{ cm}^{-1}$  versus  $0.05 \text{ cm}^{-1}$  in the weak  $\text{CO}_2$  band), both spectral sets are considered high resolution. The full set of measurements presented here is meant to simulate those that would be taken by the reflight of the Orbiting Carbon Observatory [2] after a failed launch in February 2009.

In this work the neural network cloud screen has also been extended to include radiances measured in the glint viewing mode. An OCO instrument would nominally acquire half of its measurements using sun glint in order to increase the signal-to-noise ratio over the oceans, which otherwise would be very dark in the near infrared [3].

The sampling strategy of the OCO instrument was expected to provide over one hundred thousand soundings on the day light side of each 90 minute orbit [4]. This dictates the need for a fast, robust cloud screening algorithm to populate a scene selection data base containing soundings to be processed by the  $X_{\text{CO}_2}$  inversion algorithm [5]. Previous research using statistics from the space borne Geoscience Laser Altimeter System (GLAS) indicates that roughly 15% of the global skies are clear, while approximately 20% can be classified as almost clear ( $0.0 < \tau < 0.2$ ) [6].

After the model used to calculate the full radiance spectra is introduced in Sec. 2, the principal components analysis for extracting the salient information and compressing the measurements is formulated in Sec. 3. The application of the neural network retrieval to the ensemble of synthetic radiances is discussed in Sec. 4, while Sec. 5 contains the conclusions.

## 2 MODEL

This work employs virtually the same forward model as was introduced in Part I. In order to train the neural networks, simulated radiance spectra were generated in both the nadir and glint viewing modes. The band characteristics and resolving powers are shown in Table 1. As in Part I, atmospheric profiles (12,991 in nadir and 13,495 in glint) were drawn randomly from an ECMWF data base [7], and the same World Reference System 2 (WRS-2) orbit was used for both nadir and glint viewing geometries, as shown in Fig. 1.

Table 1. Frequency windows and resolution assumed for the spectrometer.

	O <sub>2</sub> A-band	weak CO <sub>2</sub> band	strong CO <sub>2</sub> band
Minimum wavenumber ( $\text{cm}^{-1}$ )	12949.2	6166.1	4804.1
Maximum wavenumber ( $\text{cm}^{-1}$ )	13201.7	6286.4	4897.8
Nominal resolving power	17000	20000	20000
Monochromatic samples per band	26401	13001	10001
Convolved channels per band	1016	1016	1016

For the training data, land surfaces were treated as non-polarizing and non-isotropic, while oceans used a polarizing facet model [8] with a small correction for whitecaps [9]. Other simulation parameters were similar to those described in Part I and [10], including cloud, meteorology and trace gas profiles from ECMWF, as well as aerosol properties from [11]. The vertical profiles of aerosol were perturbed randomly to provide more realistic variations. The radiative transfer calculations again relied on the successive orders of interaction (SOI) code [12] [13] using the low-streams interpolater (LSI) to accelerate the calculations [14].

The model used to generate the spectra takes into account solar lines and spectral features of the surface, both of which impose a slope on each spectrum. Because these effects are unrelated to the neural network variables, they were removed from the spectra before training, according to the procedure described in [10]. Examples of spectra in the three bands are presented in Fig. 2, where the radiances, in units of photons/s/m<sup>2</sup>/sr/ $\mu\text{m}$ , are shown in red against the left

ordinate, while the solar normalized with slope removed spectra are shown in blue against the right ordinate.

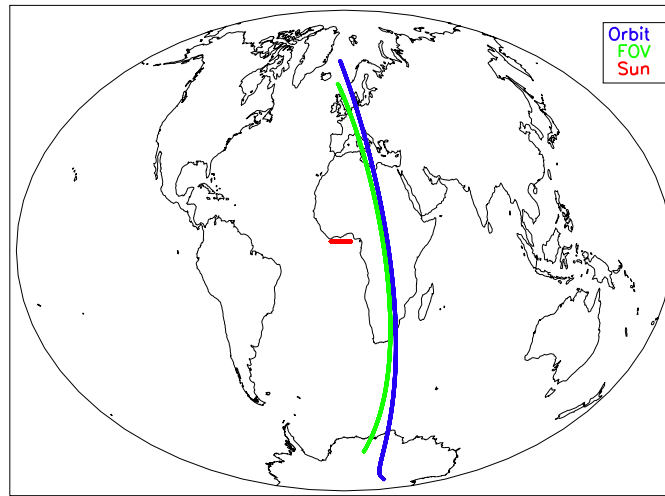


Fig. 1. The WRS-2 orbit (starting at 19:25 UTC on September 13, 2006) used in selecting surface properties for the simulations to train the neural networks. The ground track of the satellite is shown in blue, the glint target in green, and the track of the sun in red.

### 3 PRINCIPAL COMPONENTS ANALYSIS

When working with such a large number of spectral points, many of which are highly correlated, it is sensible to invoke a technique for extracting the most pertinent information from the measurements. In this work, principal components analysis (PCA) was used to reduce a correlated data set into a smaller, uncorrelated and transformed set via eigenvalue decomposition of the data covariance matrix. The matrix  $X$  containing measurements for all training profiles is first preconditioned via

$$\tilde{X}_{i,j} = \frac{(X_{i,j} - \bar{X}_j)}{\max X}, \quad (1)$$

where  $i$  labels the profile (the size varies with each training case) and  $j$  indicates the channel (1016 in each waveband). Here  $\bar{X}_j$  is the mean over all profiles of the radiance in channel  $j$ . The covariance matrix is constructed,

$$A = \tilde{X}^T \tilde{X}, \quad (2)$$

and Golub's method [15] is used to compute the singular value decomposition,

$$A = USV^T, \quad (3)$$

where the matrix  $U$  contains the data space eigenvectors of  $A$ , the matrix  $V$  contains the parameter space eigenvectors of  $A$  and the diagonal of the matrix  $S$  contain the singular values.

The fraction of variance explained by the  $k^{\text{th}}$  singular value  $s_k$  is

$$\sigma_k^2 = \frac{s_k^2}{\sum_{n=1}^N s_n^2}, \quad (4)$$

where  $N$  is the total number of singular values. The PCA algorithm is performed individually for each of the four surface types, each of the four neural network hierarchy members and for

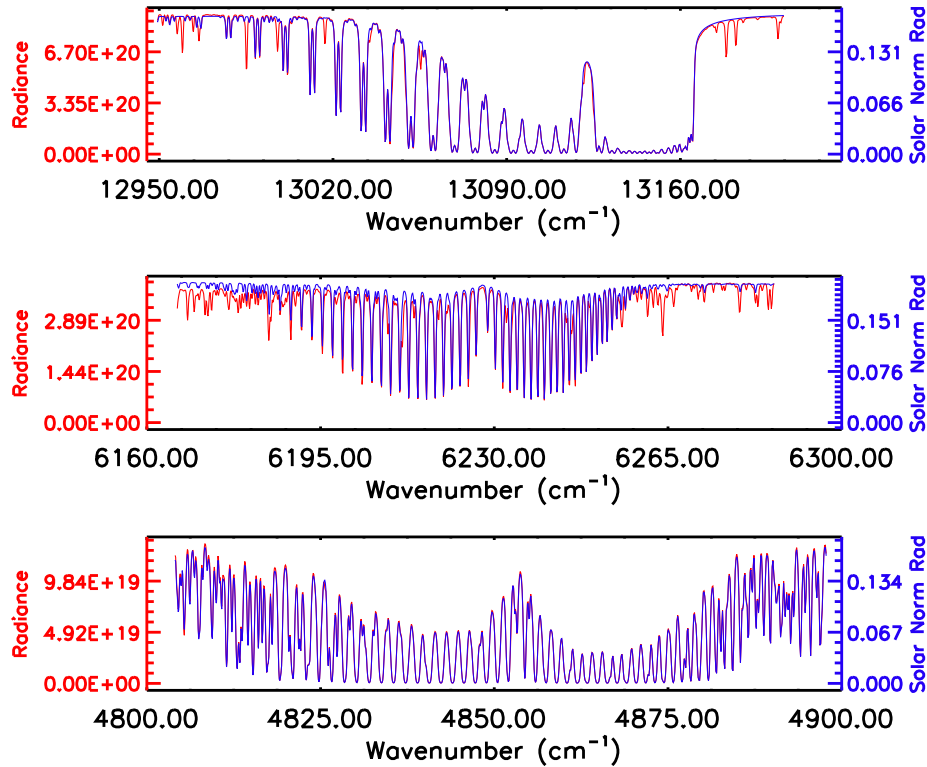


Fig. 2. Typical spectra for O<sub>2</sub> A-band (top), weak CO<sub>2</sub> band (middle) and strong CO<sub>2</sub> band (bottom). The radiances in units of photons/s/m<sup>2</sup>/sr/μm are shown in red against the left ordinate. The solar normalized spectra with slope removed are plotted in blue against the right ordinate.

each of the three wavebands. This results in 48 unique sets of EOFs, which become an inherent part of the algorithm for the inversion of cloud from the measured spectra. The stratification of scenes into desert, ice, land and ocean according to IGBP surface type is discussed in Section 4.2.1 of Part I. The notion of a hierarchy of neural networks is introduced in Section 4.2 and Table 5 of Part I; the members of a hierarchy are trained with differing total cloud amounts. Index H0 refers to the thinnest cloud cases (less than 1 gm<sup>-2</sup>), while H3 represents cases greater than 300 gm<sup>-2</sup>.

The leading singular values and the fractional variances for each of the surface types are presented in Tables 2–5 for the nadir training case. For brevity, the tables display only the four leading EOFs, rather than the five used to reconstruct the spectra in both the neural network training and inversion algorithm. In general the first EOF captures most of the variability in the spectra (95% to 100%) for all surface types, hierarchies and bands, although there are a few exceptions, notably the H0 hierarchy over desert surface in the O<sub>2</sub> A-band and strong CO<sub>2</sub> band. Typically the accumulated variability explained by the first two EOFs exceeds 99%, especially for ocean and land surfaces, while that explained by the first four exceeds 99.9%.

For illustrative purposes the normalized singular values for H0 over land surfaces are plotted against the left ordinate in the left-hand panels of Figs. 3–5, which show results for the O<sub>2</sub> A-band, weak CO<sub>2</sub> band and strong CO<sub>2</sub> band, respectively. The corresponding percentage of the variance explained by each EOF is plotted against the right ordinate. The leading eigenvectors are displayed in the right hand panels of Figs. 3–5, as functions of wavelength. They are similar in form to the original spectra, indicating that the most significant variance is due to scaling of the spectra, most likely caused by variations of surface reflectance and cloud amount over the ensemble of profiles. For the O<sub>2</sub> A-band and the weak CO<sub>2</sub> band, the rank 2 EOF is similar in

Table 2. Leading singular values and corresponding fractions of explained variance for the neural network training data for nadir mode over desert surfaces. For brevity, the results are shown only for the four leading EOFs, rather than for the five used by the neural network algorithm.

Hierarchy Index	Wave Band	$s_1$	$s_2$	$s_3$	$s_4$	$\sigma_1^2$	$\sigma_2^2$	$\sigma_3^2$	$\sigma_4^2$
0	O <sub>2</sub> -A	14.19	8.90	3.11	0.87	0.692	0.272	0.033	0.003
0	WCO <sub>2</sub>	16.73	2.56	2.00	0.43	0.963	0.023	0.014	0.001
0	SCO <sub>2</sub>	21.63	10.27	6.44	2.45	0.752	0.169	0.067	0.010
1	O <sub>2</sub> -A	25.16	5.91	2.84	0.90	0.935	0.052	0.012	0.001
1	WCO <sub>2</sub>	27.21	3.76	2.16	0.54	0.975	0.019	0.006	0.000
1	SCO <sub>2</sub>	51.78	15.10	7.87	2.68	0.899	0.076	0.021	0.002
2	O <sub>2</sub> -A	68.83	10.24	1.97	1.63	0.977	0.022	0.001	0.001
2	WCO <sub>2</sub>	82.23	3.79	2.53	0.34	0.997	0.002	0.001	0.000
2	SCO <sub>2</sub>	68.11	13.52	9.64	1.71	0.943	0.037	0.019	0.001
3	O <sub>2</sub> -A	37.52	11.69	2.07	1.18	0.908	0.088	0.003	0.001
3	WCO <sub>2</sub>	96.88	2.07	0.75	0.13	0.999	0.001	0.000	0.000
3	SCO <sub>2</sub>	73.55	6.66	3.52	0.77	0.989	0.008	0.002	0.000

Table 3. Same as in Table 2, except for permanent snow and ice surfaces.

Hierarchy Index	Wave Band	$s_1$	$s_2$	$s_3$	$s_4$	$\sigma_1^2$	$\sigma_2^2$	$\sigma_3^2$	$\sigma_4^2$
0	O <sub>2</sub> -A	27.50	6.40	1.85	0.82	0.944	0.051	0.004	0.001
0	WCO <sub>2</sub>	30.99	2.83	1.56	0.45	0.989	0.008	0.002	0.000
0	SCO <sub>2</sub>	31.02	6.15	5.51	1.70	0.930	0.036	0.029	0.003
1	O <sub>2</sub> -A	28.17	2.35	1.11	0.37	0.991	0.007	0.002	0.000
1	WCO <sub>2</sub>	34.85	0.70	0.65	0.13	1.000	0.000	0.000	0.000
1	SCO <sub>2</sub>	25.78	3.23	1.87	0.58	0.978	0.015	0.005	0.000
2	O <sub>2</sub> -A	22.39	2.96	0.74	0.59	0.981	0.017	0.001	0.000
2	WCO <sub>2</sub>	66.15	3.88	1.49	0.26	0.996	0.003	0.001	0.000
2	SCO <sub>2</sub>	56.46	13.04	5.89	1.91	0.938	0.050	0.010	0.001
3	O <sub>2</sub> -A	42.26	3.88	0.60	0.30	0.991	0.008	0.000	0.000
3	WCO <sub>2</sub>	35.49	1.42	0.31	0.07	0.998	0.002	0.000	0.000
3	SCO <sub>2</sub>	29.35	4.44	1.26	0.67	0.975	0.022	0.002	0.001

Table 4. Same as in Table 2, except for ocean surfaces.

Hierarchy Index	Wave Band	$s_1$	$s_2$	$s_3$	$s_4$	$\sigma_1^2$	$\sigma_2^2$	$\sigma_3^2$	$\sigma_4^2$
0	O <sub>2</sub> -A	60.30	6.55	1.88	1.07	0.987	0.012	0.001	0.000
0	WCO <sub>2</sub>	77.45	1.57	0.95	0.18	0.999	0.001	0.000	0.000
0	SCO <sub>2</sub>	62.63	5.39	3.61	0.91	0.989	0.007	0.003	0.000
1	O <sub>2</sub> -A	120.0	7.70	1.10	0.97	0.996	0.004	0.000	0.000
1	WCO <sub>2</sub>	167.4	2.80	1.84	0.22	1.000	0.000	0.000	0.000
1	SCO <sub>2</sub>	138.8	11.45	7.23	1.45	0.990	0.007	0.003	0.000
2	O <sub>2</sub> -A	174.7	15.71	2.18	1.99	0.992	0.008	0.000	0.000
2	WCO <sub>2</sub>	235.7	5.81	2.76	0.44	0.999	0.001	0.000	0.000
2	SCO <sub>2</sub>	170.9	19.83	10.27	2.13	0.983	0.013	0.004	0.000
3	O <sub>2</sub> -A	171.9	17.10	2.77	1.45	0.990	0.010	0.000	0.000
3	WCO <sub>2</sub>	188.3	4.05	1.04	0.21	1.000	0.000	0.000	0.000
3	SCO <sub>2</sub>	146.7	11.75	4.50	1.40	0.993	0.006	0.001	0.000

Table 5. Same as in Table 2, except for land surfaces.

Hierarchy Index	Wave Band	$s_1$	$s_2$	$s_3$	$s_4$	$\sigma_1^2$	$\sigma_2^2$	$\sigma_3^2$	$\sigma_4^2$
0	O <sub>2</sub> -A	72.04	15.48	4.55	1.01	0.952	0.044	0.004	0.000
0	WCO <sub>2</sub>	88.06	4.00	2.66	0.68	0.997	0.002	0.001	0.000
0	SCO <sub>2</sub>	73.11	15.54	6.94	2.74	0.947	0.043	0.009	0.001
1	O <sub>2</sub> -A	94.28	10.27	3.81	1.35	0.986	0.012	0.002	0.000
1	WCO <sub>2</sub>	119.7	4.88	3.13	0.61	0.998	0.002	0.000	0.000
1	SCO <sub>2</sub>	102.6	21.71	11.76	3.14	0.944	0.042	0.012	0.001
2	O <sub>2</sub> -A	175.8	20.41	3.21	2.93	0.986	0.013	0.000	0.000
2	WCO <sub>2</sub>	212.2	6.58	4.19	0.54	0.999	0.001	0.000	0.000
2	SCO <sub>2</sub>	146.2	24.00	15.98	2.68	0.962	0.026	0.011	0.000
3	O <sub>2</sub> -A	113.6	22.16	3.35	2.15	0.962	0.037	0.001	0.000
3	WCO <sub>2</sub>	183.1	3.79	1.38	0.22	1.000	0.000	0.000	0.000
3	SCO <sub>2</sub>	138.6	11.90	6.19	1.36	0.990	0.007	0.002	0.000

shape to the inverse of the original spectrum, as would be caused by variations in cloud height and cloud type, both of which stretch and compress the spectra. The higher rank EOFs are more difficult to interpret physically, but presumably are associated with variations in atmospheric and cloud properties, such as effective radii and phase matrices. However, the higher EOFs are closely centered around the zero line, indicating that they capture little variability of the spectra.

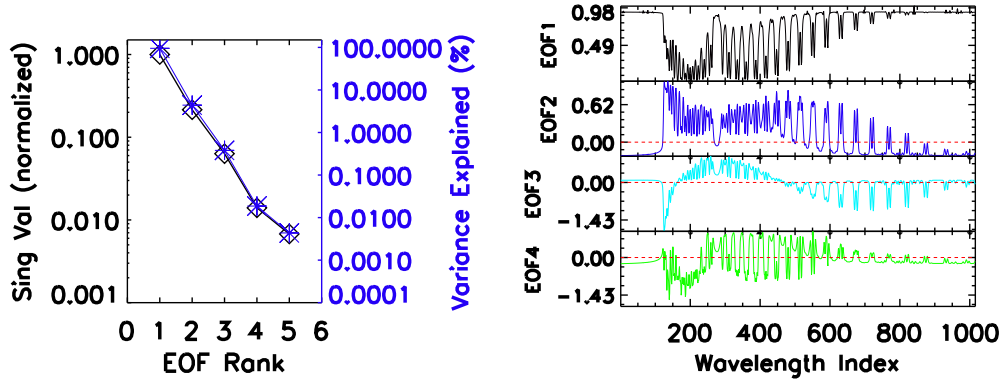


Fig. 3. Results from principal component analysis on the O<sub>2</sub> A-band for hierarchy index 0 and land surfaces only. The left panel shows the five leading normalized singular values plotted against the left ordinate, and the percent variance explained against the right ordinate. The right panels show the leading EOFs versus the wavelength index. Only four EOFs (rather than five) are displayed to enhance the size of the images. The red, horizontal lines indicate the zero levels of the EOFs.

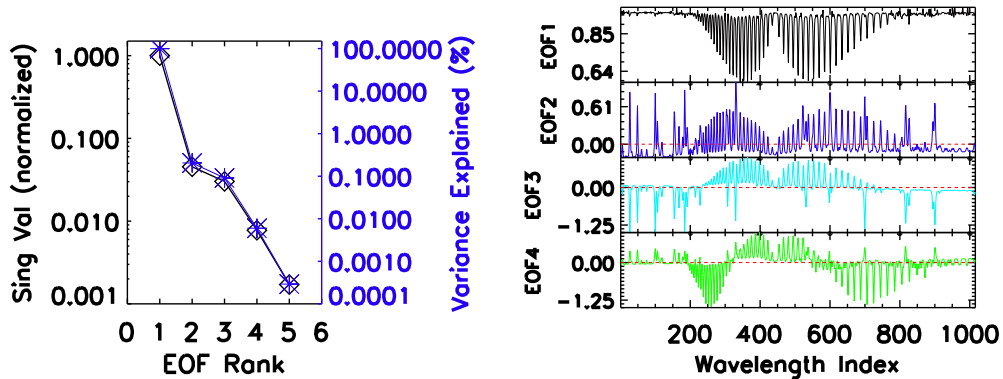


Fig. 4. Same as in Fig. 3, except for the weak CO<sub>2</sub> band.

Projections of the spectra onto the leading EOFs (projected objects, or *ProjObj* for short) are used by the neural networks to make predictions of the cloud properties. Hence, a full spectrum of 1016 channels per waveband is reduced by PCA to just five values per waveband. This reduction of the input data set by two and a half orders of magnitude into orthonormal form more distinctly separates it into classes that can be identified by the neural network. Figure 6 shows examples of *ProjObj* for clear sky (top row), a moderately thin water cloud (middle row) and a moderately thick mixed phase cloud (bottom row) for the O<sub>2</sub> A-band (left column), the weak CO<sub>2</sub> band (middle column) and the strong CO<sub>2</sub> band (right column). PCA of sun-glint training data provides virtually the same patterns as the nadir data; therefore, plots and tables for sun-glint are omitted.

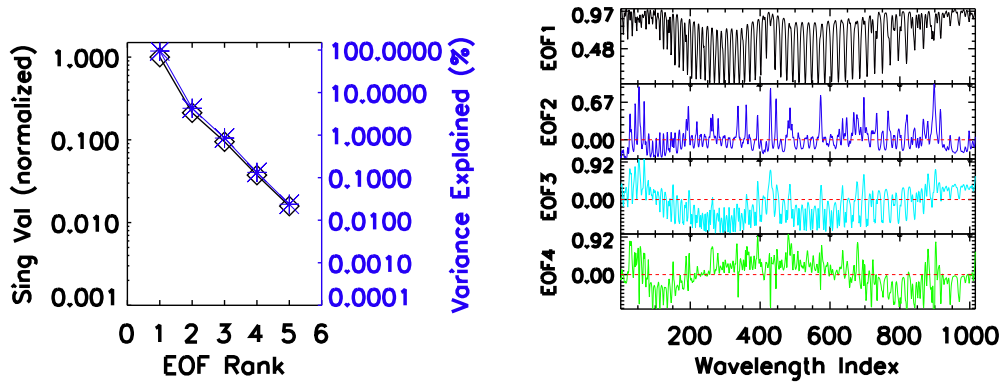


Fig. 5. Same as in Fig. 3, except for the strong CO<sub>2</sub> band.

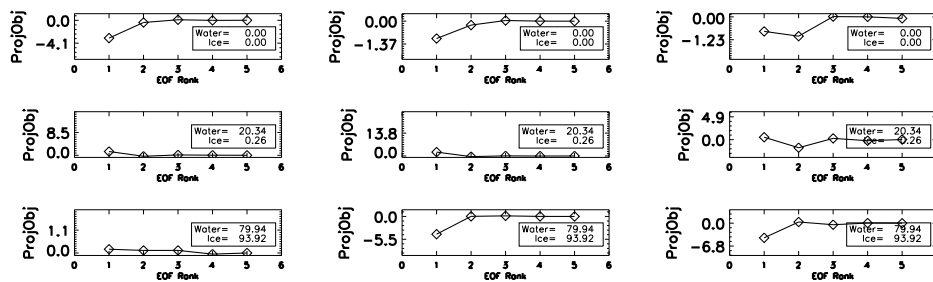


Fig. 6. Projections of the spectra onto the five leading EOFs (*ProjObj*) for clear sky (top), moderately thin water cloud (middle) and a moderately thick mixed phase cloud (bottom). The columns represent the O<sub>2</sub> A-band (left), weak CO<sub>2</sub> band (middle) and strong CO<sub>2</sub> band (right). The legends shows the water and ice amounts in gm<sup>-2</sup>.

#### 4 NEURAL NETWORK RETRIEVALS

The architecture of the two layer feed forward neural network and the determination of the network parameters was described extensively in Part I. Briefly, weights and biases are determined iteratively by minimizing a cost function representing the difference between the predicted and target results. The only difference between the network discussed there and the one presented here is that the spectra have been replaced with the *ProjObj*, giving fifteen predictors representing the three wavebands. The remaining predictor variables (solar zenith angle, surface pressure, surface reflectance and mean atmospheric temperature) have not changed, yielding a total of nineteen predictors per sounding (so  $P = 19$  in the notation of Section 3.2.6 of Part I). The resulting weights and biases, along with the EOFs and other normalization variables from training, are used to map inputs onto the five output target variables; cloud water ( $c_w$ ), cloud ice ( $c_i$ ), effective scattering heights of cloud water and ice, ( $p_{cw}$  and  $p_{ci}$ , respectively) and the column water vapor ( $w$ ). Therefore,  $T = 5$  in the notation of Section 3.2.6 of Part I. Note too, that  $N = 10$  nodes were used in the neural network training here, yielding  $W = N(P + T) = 240$  weights and  $b = N + T = 15$  biases for the two-layer model.

The dominant instrument noise was assumed to be photon noise, although a model was used that accounted for the secondary effects of background noise. The noise  $N$  and radiance  $I$  were related by

$$N = I_0 \sqrt{c_p^2 (I/I_0) + c_b^2}, \quad (5)$$

Table 6. Values used for simulating instrument noise. The units of  $I_0$  are photons/s/m<sup>2</sup>/sr/μm.

	O <sub>2</sub> A-band	weak CO <sub>2</sub> band	strong CO <sub>2</sub> band
$I_0$	1.4E19	4.9E18	1.7E18
$c_p$	0.0070	0.0073	0.0095
$c_b$	0.0149	0.0120	0.0328

where  $c_p$  and  $c_b$  are pixel-dependent coefficients for the photon and background noise, respectively, and  $I_0$  is a reference radiance. Table 6 shows for the three bands the reference radiance and corresponding coefficients (averaged over all pixels) determined in the pre flight thermal vacuum chamber tests performed on the OCO instrument. The uncertainties in the remaining predictor variables, surface pressure, surface reflectance and mean temperature, were drawn randomly from Gaussian populations with zero means and standard deviations of 2%, 10% and 2% of the climatological values, as described in Part I. These uncertainties, along with measurement noise, were used to address the sensitivity of the neural networks to errors in the predictors, to be discussed in the following section.

#### 4.1 Hold-Over data set

Hold-over subsets were extracted from the full ensemble of training profiles for both nadir and glint viewing geometries as well as the four surface types prior to splitting into the four hierarchy members. Hence, it is implicit that all model settings are the same between the training and hold-over sets. Performing retrievals on the hold-over data set therefore provides a test of the trickle-down method, as described in Part I.

Contingency tables are used to quantify the retrieval skill. Two important measures are the accuracy (*ACC*) and the positive predictive value (*PPV*). The first is defined in Section 4.2.3 of Part I to be the fraction

$$ACC = (TP + TN)/(P + N),$$

where  $P$  is the number of clear cases,  $N$  is the number of cloudy,  $TP$  are the correctly classified clear and  $TN$  are the correctly classified cloudy. The second is

$$PPV = TP/(TP + FP),$$

where  $FP$  are the incorrectly classified clear cases, i.e., cloudy cases that are estimated by the neural network to be clear. As in Part I, the threshold between clear and cloudy is defined to be 2 gm<sup>-2</sup> and 10 gm<sup>-2</sup> for cloud water and cloud ice, respectively.

##### 4.1.1 Nadir Results

Scatter plots of the predicted versus true cloud amounts for the hold-over data set in nadir viewing mode using the four-member hierarchy are plotted in Fig. 7. Each color represents one of the four surface types, desert, ice, land and ocean. For the retrieval of cloud water (left panel) the correlation coefficients are high ( $R > 0.9$ ) for all but ice surfaces, which consistently, but incorrectly, relied on hierarchy member H3 (trained with total cloud water plus ice in excess of 300 gm<sup>-2</sup>), regardless of the true cloud amount. For retrievals of cloud ice (right panel) there is more scatter for all surface types ( $R = 0.66, 0.81, 0.81$  for ocean, land and desert, respectively). Again, the horizontal striations are caused by incorrect selection of the hierarchy member. As with cloud water, retrievals over ice surfaces are very poor.

In Part I the hierarchy trickle-down concept was introduced as a method to increase the accuracy of the retrieved cloud amounts, especially for the thin cloud cases. It was shown there that this technique proves quite useful in this respect, but that it does not fully eliminate the problem of decreasing accuracy with decreasing cloud amount, an issue that persists in these

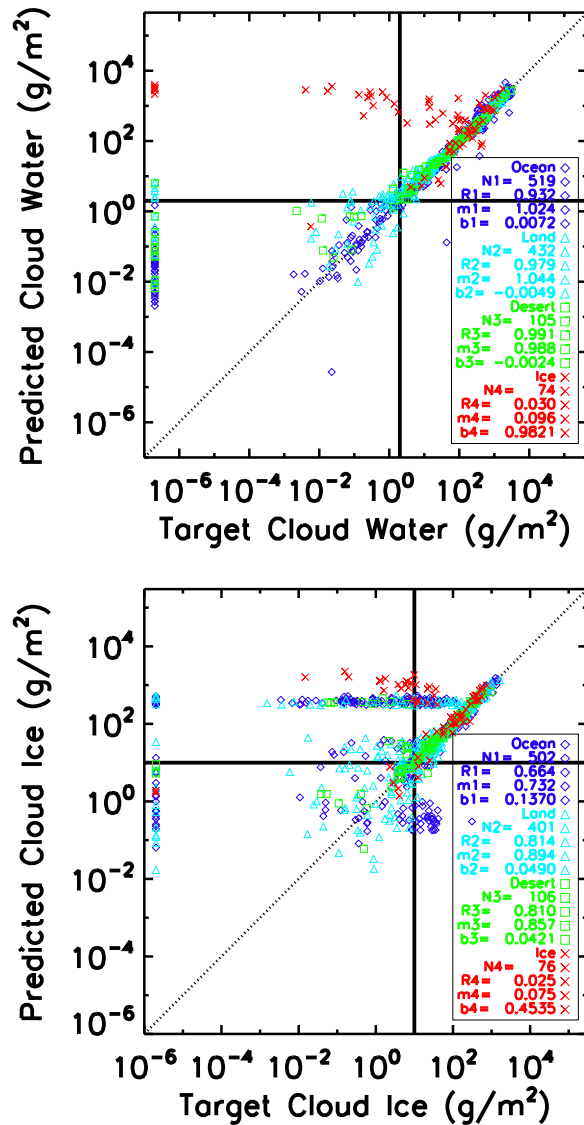


Fig. 7. Neural network predicted vs target values of cloud water (top) and cloud ice (bottom) in nadir mode over the four surface types on the hold-over data set without uncertainties added. The linear regression coefficient ( $R$ ), slope ( $m$ ) and bias ( $b$ ) are given in the legends, along with the number of data points ( $N$ ). The horizontal and vertical bisection lines indicate the chosen thresholds of  $2 \text{ gm}^{-2}$  (cloud water) and  $10 \text{ gm}^{-2}$  (cloud ice) for distinguishing cloudy scenes from clear.

results. Fortunately, since the primary function of the neural network is to provide a way to discriminate clear from cloudy scenes, the actual estimated value of cloud amount for the thin cases is not critical. However, for the purpose of analysis and to gain insight into the algorithm, it is useful to present and discuss these quantities rather than simply the binary cloudy/clear flags from the final threshold test.

The contingency tables for the nadir, hold-over retrievals are shown in Table 7. Relatively high true positive rates ( $TPRs$ ), coupled with low false positive rates ( $FPRs$ ) yield accuracies in the 70% to 99% range and  $PPVs$  ranging from 66% to 100%. These values are similar to those reported in Part I for nadir mode.

Table 7. Contingency tables for classifications on the hold-over data set for cloud water and ice in nadir viewing mode without uncertainties added (corresponding to Fig. 7). The results are shown for both cloud water and cloud ice for the four surface types.

Surface	Cloud	Clear atmospheres					Cloudy atmospheres					ACC	PPV
		Total cases	Predicted clear		Predicted cloudy		Total cases	Predicted clear		Predicted cloudy			
			#	TPR	#	FNR		#	FPR	#	TNR		
Desert	Water	28	25	89%	3	11%	77	0	0%	77	100%	97%	100%
Desert	Ice	43	30	70%	13	30%	63	2	3%	61	97%	86%	94%
Ice	Water	21	2	10%	19	90%	53	1	2%	52	98%	73%	67%
Ice	Ice	30	14	47%	16	53%	46	2	4%	44	96%	76%	88%
Land	Water	110	88	80%	22	20%	322	1	0%	321	100%	95%	99%
Land	Ice	156	110	71%	46	29%	245	9	4%	236	96%	86%	92%
Ocean	Water	129	127	98%	2	2%	390	3	1%	387	99%	99%	98%
Ocean	Ice	178	61	34%	117	66%	324	32	10%	292	90%	70%	66%

Table 8. Contingency tables for classifications on the hold-over data set for cloud water and ice in nadir viewing mode with uncertainties added (corresponding to Fig. 8).

Surface	Cloud	Clear atmospheres					Cloudy atmospheres					ACC	PPV
		Total cases	Predicted clear		Predicted cloudy		Total cases	Predicted clear		Predicted cloudy			
			#	TPR	#	FNR		#	FPR	#	TNR		
Desert	Water	28	22	79%	6	21%	77	1	1%	76	99%	93%	96%
Desert	Ice	36	24	67%	12	33%	62	1	2%	61	98%	87%	96%
Ice	Water	21	1	5%	20	95%	52	3	6%	49	94%	68%	25%
Ice	Ice	30	14	47%	16	53%	46	2	4%	44	96%	76%	88%
Land	Water	110	81	74%	29	26%	308	3	1%	305	99%	92%	96%
Land	Ice	150	92	61%	58	39%	241	22	9%	219	91%	80%	81%
Ocean	Water	129	123	95%	6	5%	390	3	1%	387	99%	98%	98%
Ocean	Ice	178	60	34%	118	66%	325	34	10%	291	90%	70%	64%

The sensitivity of the retrieval to uncertainties in surface albedo, surface pressure, temperature profile and measurement noise was tested by adding perturbations to the predictors, as described in Part I. Scatter plots for the nadir retrievals with uncertainties added are shown in Fig. 8. Although it is evident that there is a significant increase in scatter, and hence decrease in correlation, for both cloud water (left) and cloud ice (right) when compared to Fig. 7, the overall classification of scenes as either cloudy or clear is hardly affected, as can be seen by comparing the contingency tables (Table 8 and Table 7). Typically the ACCs and PPVs decrease only by about 2 to 3% due to the addition of errors. Overall these results indicate that the neural network algorithm provides a reasonably reliable method for distinguishing clear from cloudy scenes in the nadir viewing mode over most surface types.

#### 4.1.2 Glint Results

Similarly, Fig. 9 shows the scatter plots from retrievals using glint viewing geometry on the hold-over data for the four surface types. The corresponding contingency tables are presented in Table 9. The correlations in glint mode over desert and land surfaces are very similar to those in nadir mode, while the retrievals over ice surfaces are still poor. However, the correlations over ocean are significantly lower than in nadir mode, presumably because cloud is hard to

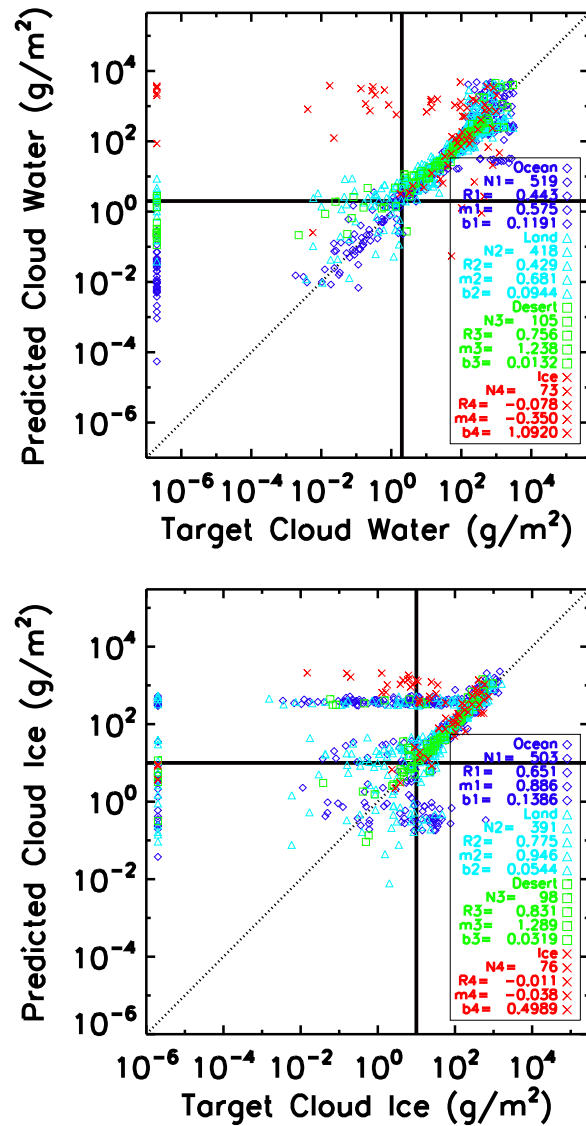


Fig. 8. Same as Fig. 7, except uncertainties were added to the predictors before performing the retrievals.

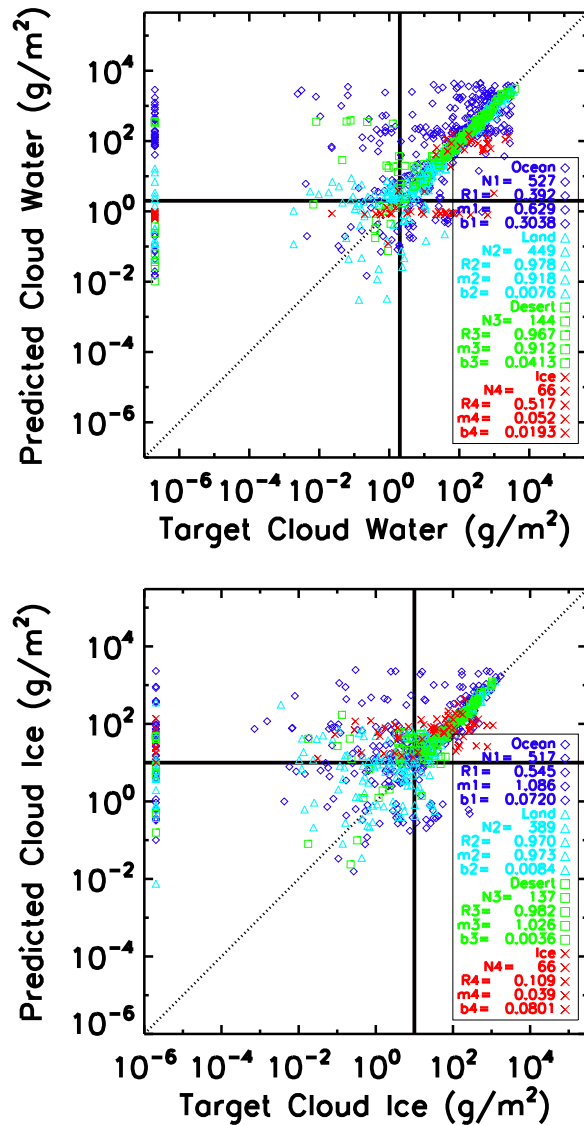


Fig. 9. Neural network predicted versus target values of cloud water (top) and cloud ice (bottom) in glint viewing geometry over the four surface types on the hold-over data set without uncertainties added. The linear regression coefficient ( $R$ ), slope ( $m$ ) and bias ( $b$ ) are given in the legends, along with the number of data points ( $N$ ). The horizontal and vertical bisection lines indicate the chosen thresholds of  $2 \text{ gm}^{-2}$  (cloud water) and  $10 \text{ gm}^{-2}$  (cloud ice) for distinguishing cloudy scenes from clear.

distinguish against the bright ocean surface when viewing sun-glint. This is especially true for the retrieval of cloud ice, where the H3 hierarchy member is consistently chosen no matter the true value of cloud amount.

Although the scatter in the retrieved values is large, the contingency tables show that the retrieval skill is comparable to that for the nadir mode. Over land and ocean surfaces the values of ACC are in the range 65% to 89%, while the PPVs are in the range 76% to 88%, indicating that the majority of the profiles are correctly classified and that most of the scenes identified as clear are in fact clear. Because glint measurements over ocean, with their high signal-to-noise ratio, are potentially very important for the retrieval of  $X_{\text{CO}_2}$  from an OCO-like instrument [3],

Table 9. Contingency tables for classifications on the hold-over data set for cloud water and ice in glint mode without uncertainties added (corresponding to Fig. 9). The results are shown for both cloud water and cloud ice for the four surface types.

Surface	Cloud	Clear atmospheres					Cloudy atmospheres					ACC	PPV
		Total cases	Predicted clear		Predicted cloudy		Total cases	Predicted clear		Predicted cloudy			
			#	TPR	#	FNR		#	FPR	#	TNR		
Desert	Water	37	22	59%	15	41%	107	1	1%	106	99%	89%	96%
Desert	Ice	43	17	40%	26	60%	94	4	4%	90	96%	78%	81%
Ice	Water	26	25	96%	1	4%	40	16	40%	24	60%	74%	61%
Ice	Ice	24	1	4%	23	96%	42	0	0%	42	100%	65%	100%
Land	Water	130	94	72%	36	28%	319	23	7%	296	93%	87%	80%
Land	Ice	141	99	70%	42	30%	248	13	5%	235	95%	86%	88%
Ocean	Water	132	59	45%	73	55%	394	19	5%	375	95%	83%	76%
Ocean	Ice	209	105	50%	104	50%	308	29	9%	279	91%	74%	78%

Table 10. Contingency tables for classifications on the hold-over data set for cloud water and ice in glint mode with uncertainties added (corresponding to Fig. 10). The results are shown for four surface types.

Surface	Cloud	Clear atmospheres					Cloudy atmospheres					ACC	PPV
		Total cases	Predicted clear		Predicted cloudy		Total cases	Predicted clear		Predicted cloudy			
			#	TPR	#	FNR		#	FPR	#	TNR		
Desert	Water	37	20	54%	17	46%	107	2	2%	105	98%	87%	91%
Desert	Ice	46	18	39%	28	61%	94	6	6%	88	94%	76%	75%
Ice	Water	26	25	96%	1	4%	40	17	42%	23	57%	73%	60%
Ice	Ice	24	1	4%	23	96%	42	0	0%	42	100%	65%	100%
Land	Water	130	106	82%	24	18%	319	18	6%	301	94%	91%	85%
Land	Ice	144	93	65%	51	35%	250	18	7%	232	93%	82%	84%
Ocean	Water	132	62	47%	70	53%	395	25	6%	370	94%	82%	71%
Ocean	Ice	209	101	48%	108	52%	307	30	10%	277	90%	73%	77%

it is desirable to increase the skill of the cloud screening for this scenario. One option to be explored is to further segregate the training data into distinct cloud types prior to neural network training.

Figure 10 shows scatter plots of the predicted versus target values in glint mode when the predictors are subject to uncertainties. The corresponding contingency tables are shown in Table 10. Both ACC and PPV change by only a few percent when uncertainties are added, consistent with the results for nadir mode. Thus, the neural network algorithm appears to be robust with respect to the addition of realistic uncertainties.

## 4.2 Independent data set

An independent data set was generated using a model that relied on CloudSat and Calipso profiles for the cloud and aerosol properties. The surface model over land was changed from unpolarized to polarized for these simulations, while the surface model over ocean remained the same. Furthermore the Goddard Space Flight Center (GSFC) parametrized chemistry and transport model (PCTM) [16] was used to provide realistic variations in the CO<sub>2</sub> field. All other model parameters were held fixed, including the spectroscopy data base, instrument line shape functions and all settings used in the radiative transfer model. In order to provide global

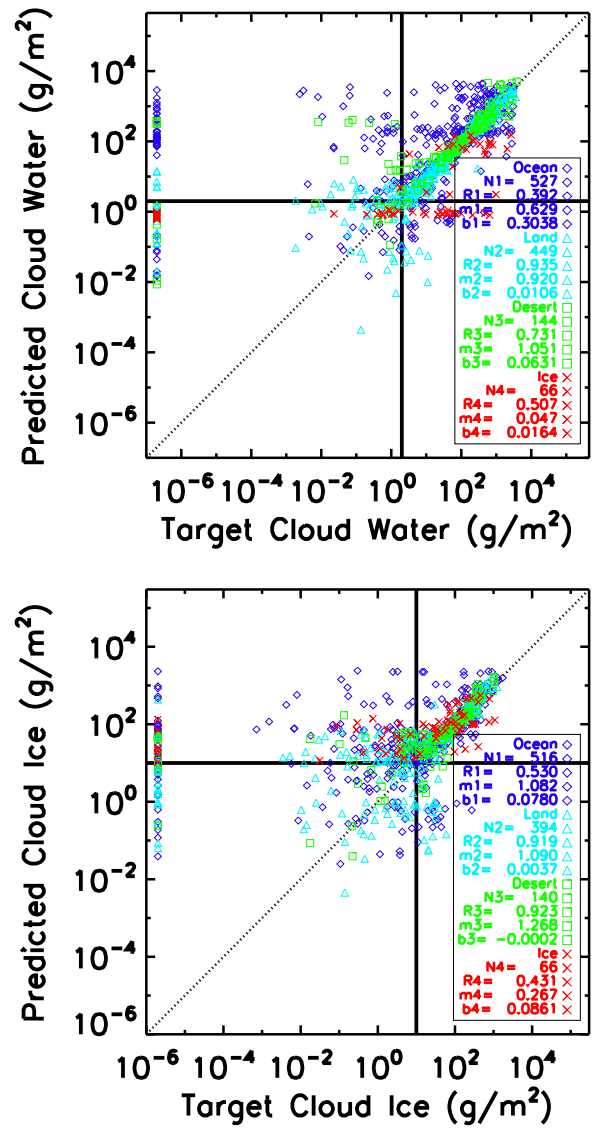


Fig. 10. Same as Fig. 9, except uncertainties were added to the predictors before performing the retrievals.

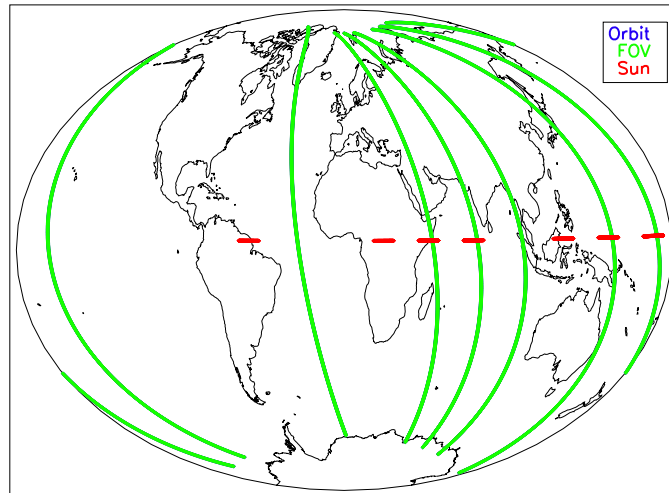


Fig. 11. The WRS-2 orbits (starting at 19:25 UTC on September 13, 2006) used in selecting surface properties for the neural network independent data set. In nadir mode the ground track of the satellite and the field of view (green) overlap. The track of the sun during each orbit is displayed in red, and is always approximately 20 degrees to the west of the ground track.

variations in the surface properties, simulations over multiple orbits were performed, as shown in Fig. 11.

Histograms of cloud, atmosphere and surface properties from the independent data set are displayed in Fig. 12 and Fig. 13. In these histograms 4995 scenes (55% of total) completely free of cloud water and 2361 (26% of total) free of cloud ice have been omitted for clarity. These cloud free scenes are indicated by cases with scattering heights equal to zero in the lower panels of Fig. 12. Also, for clarity in plotting, scenes with cloud amounts greater than  $1000.0 \text{ gm}^{-2}$  have been reassigned to this value; 30 scenes in total for cloud water and 100 for cloud ice. In general the histograms of the atmospheric and surface parameters are similar to those for the training data set, shown in Figs. 2 and 3 of Part I.

#### 4.2.1 Nadir Results

The results of the neural network predictions of cloud water and cloud ice on the independent data set in nadir mode for the four surface types are shown in Fig. 14. Uncertainties were added to the predictors before retrieval. The patterns in the independent retrievals are similar to those for the hold-over data set; that is, the accuracy of retrieved cloud water and ice is reasonable when the true values lie above the thresholds of  $2 \text{ gm}^{-2}$  and  $10 \text{ gm}^{-2}$  respectively, but degrades significantly with decreasing cloud amount. The results vary somewhat with surface type. For cloud ice retrievals the horizontal striations in the estimated values are caused by incorrect selection of the hierarchy member for the final retrieval.

Comparing the contingency table for the independent nadir retrievals (Table 11) with the hold-over results (Table 8) shows that the accuracy (*ACC*) is typically much worse for all cases, while the positive predictive value (*PPV*) shows varying levels of improvement in all but one case (ice clouds over ice surfaces). The combination of moderately low *ACC* with very high *PPV* indicates that many clear scenes are inadvertently being rejected as cloudy, but that almost all of the scenes flagged as clear are in fact clear. As with the hold-over data set, the classification skill typically is better for cloud water than for cloud ice. Note that the retrieval skill is significantly worse over ice surfaces relative to the other surface types, presumably due to the difficulty in distinguishing bright ice and snow surfaces from bright clouds.

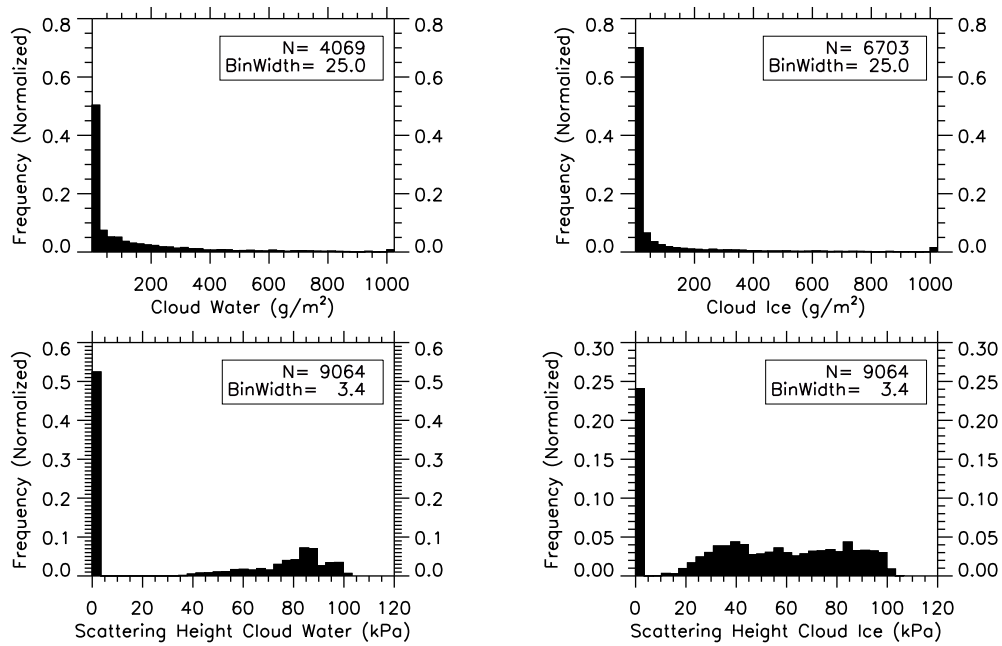


Fig. 12. Histograms of cloud water (upper left), cloud ice (upper right), effective scattering height of cloud water (lower left) and effective scattering height of cloud ice (lower right) derived from the profiles used for the independent testing.

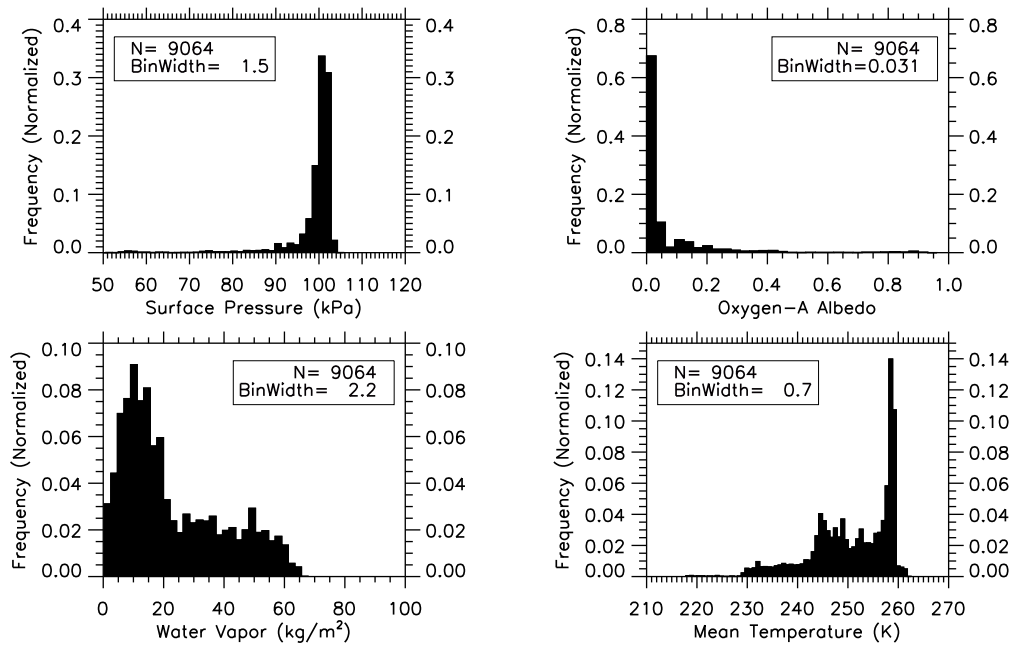


Fig. 13. Histograms of surface pressure (upper left), O<sub>2</sub> A-band surface albedo (upper right), column water vapor (lower left) and mean temperature (lower right) derived from the profiles used for independent testing.

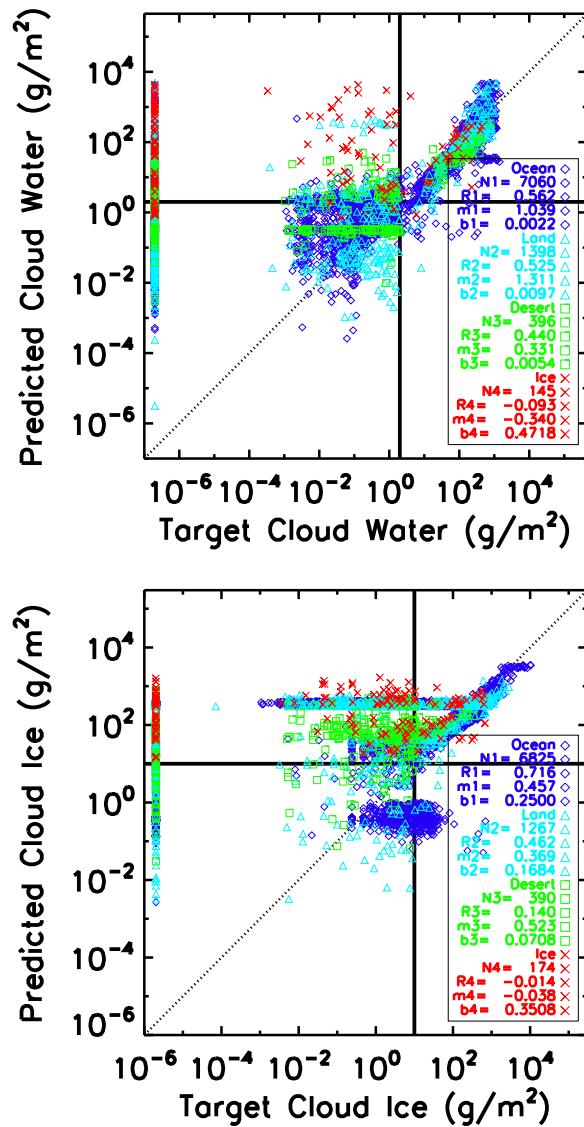


Fig. 14. Neural network predicted versus target values of cloud water (top) and cloud ice (bottom) in nadir mode over the four surface types on the independent data set. The linear regression coefficient ( $R$ ), slope ( $m$ ) and bias ( $b$ ) are given in the legends, along with the number of data points ( $N$ ). The horizontal and vertical bisection lines indicate the chosen thresholds of  $2 \text{ gm}^{-2}$  (cloud water) and  $10 \text{ gm}^{-2}$  (cloud ice) for distinguishing cloudy scenes from clear.

Table 11. Contingency tables for classifications on the independent data set (corresponding to Fig. 14) for cloud water and ice in nadir viewing mode. The results are shown separately for the four surface types.

Surface	Cloud	Clear atmospheres					Cloudy atmospheres					ACC	PPV
		Total cases	Predicted clear		Predicted cloudy		Total cases	Predicted clear		Predicted cloudy			
			#	TPR	#	FNR		#	FPR	#	TNR		
Desert	Water	350	243	69%	107	31%	46	0	0%	46	100%	73%	100%
Desert	Ice	357	101	28%	256	72%	33	2	6%	31	94%	34%	98%
Ice	Water	115	15	13%	100	87%	30	4	13%	26	87%	28%	79%
Ice	Ice	127	9	7%	118	93%	47	5	11%	42	89%	29%	64%
Land	Water	1054	682	65%	372	35%	344	12	4%	332	96%	73%	98%
Land	Ice	892	393	44%	499	56%	375	20	5%	355	95%	59%	95%
Ocean	Water	5239	3852	74%	1387	26%	1821	44	2%	1777	98%	80%	99%
Ocean	Ice	4766	750	16%	4016	84%	2059	205	10%	1854	90%	38%	79%

For completeness the scatter plots of the effective scattering heights of cloud water and cloud ice, as well as water vapor, in nadir mode for the independent data set are shown in Fig. 15. It is evident that the retrieval accuracies of the effective scattering heights are less than ideal. Of particular concern is the wide range of retrieved values when the scene is completely cloud free, i.e., cases with target scattering heights identically zero. The accuracies in the column water vapor amount also have large variations, although the linear correlations indicate that there is some information in the retrieved values. As was explained in Part I, these variables have been retained in the current version of the algorithm because it was found that removing them from the set of target variables did not actually increase the accuracy in the prediction of the cloud water and ice amounts. Furthermore, it is hoped that future improvements to the algorithm will lead to reasonable retrievals of these quantities which, along with the estimated values of cloud water and ice, can then be used as inputs to constrain the  $X_{CO_2}$  inversion algorithm [5] and [17]. It should be noted however, that removal of these variables from the algorithm would significantly reduce the size of the network architecture (see Sec. 3.2.6 of Part I), thereby allowing for an increase in the number of nodes in the hidden layer, which leads to a decrease in the mean squared error in the retrieved parameters. Future testing will explore possible improvements via removal of these parameters.

#### 4.2.2 Glint Results

The results from the glint mode retrievals with uncertainties added are shown in Fig. 16. The scatter is significantly higher than in nadir viewing mode, and for ice clouds incorrect selection of the hierarchy member is common, causing many clear scenes to be classified as cloudy, leading to moderately low accuracy. Fortunately, for both cloud water and ice the retrieval tends to overestimate, thus keeping the value of *PPV* high, and ensuring that scenes classified as clear usually are clear. The corresponding contingency tables (Table 12), when compared to the hold-over results presented in Table 10 corroborate these findings. As in nadir, for glint mode the *ACC* is typically much worse, while improvements to the *PPV* are very noticeable on the independent data set.

Again for completeness, the retrieved values of the effective scattering heights of cloud water and cloud ice and the column water vapor amount are shown for the glint mode retrieval on the independent data set in Fig. 17. Overall the correlations are low for these variables as was the case in the nadir mode, although for water vapor there is clearly some information in the retrieved value. As discussed in the previous section, it is hoped that future modifications to the retrieval algorithm will yield increased accuracy in these variables, allowing them to be used as first guess information in the  $X_{CO_2}$  inversion algorithm.

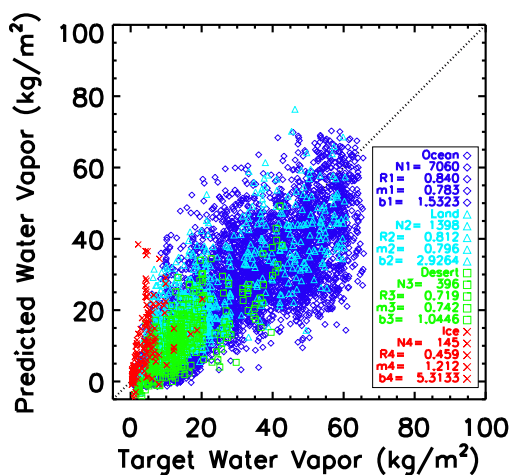
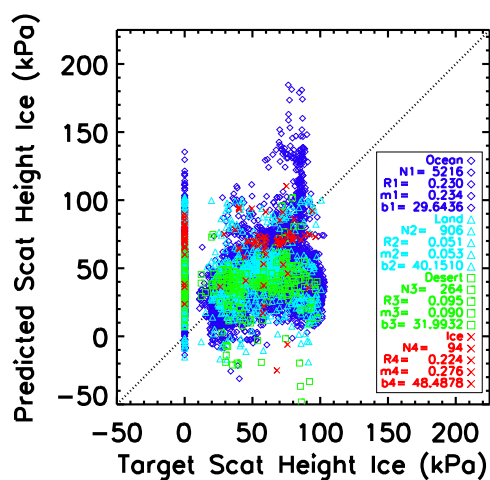
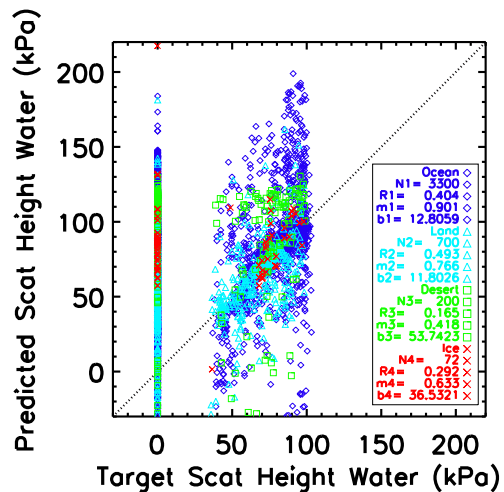


Fig. 15. Neural network predicted versus target values of effective scattering height of cloud water (top) and effective scattering height cloud ice (middle) and column water vapor (bottom) in nadir mode over the four surface types on the independent data set. The linear regression coefficient ( $R$ ), slope ( $m$ ) and bias ( $b$ ) are given in the legends, along with the number of data points ( $N$ ).

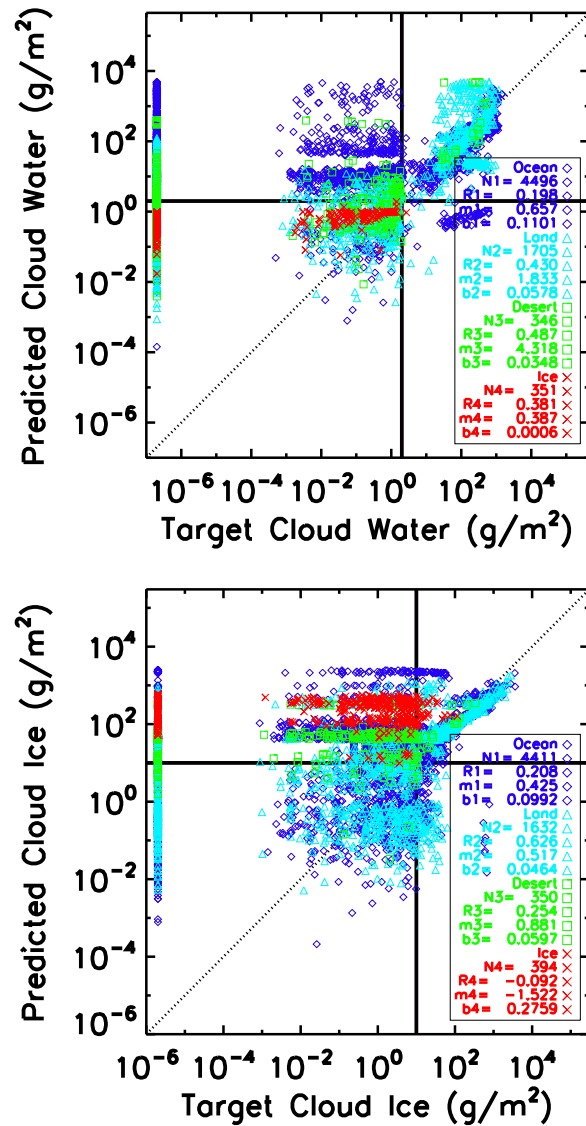


Fig. 16. Same as in Fig. 14, except for glint viewing geometry.

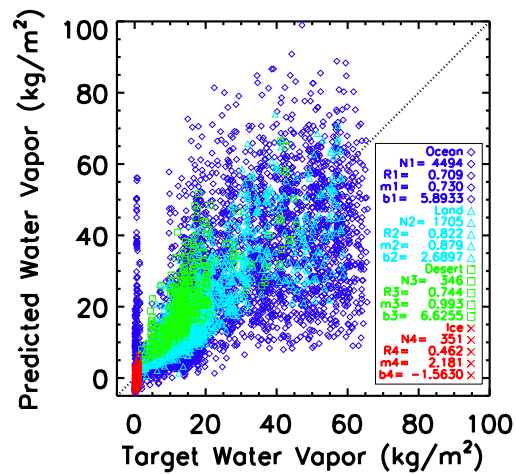
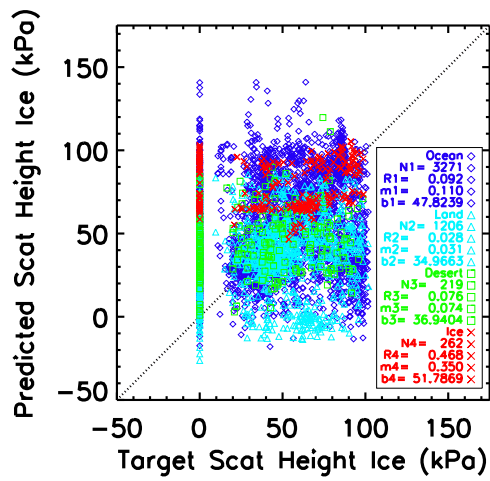
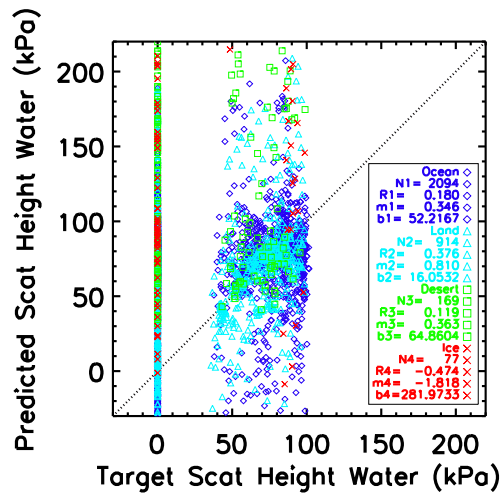


Fig. 17. Same as in Fig. 15, except for glint viewing geometry.

Table 12. Contingency tables for classifications on the independent data set (corresponding to Fig. 16) for cloud water and ice in glint viewing geometry. The results are shown separately for the four surface types.

Surface	Cloud	Clear atmospheres					Cloudy atmospheres					ACC	PPV
		Total cases	Predicted clear		Predicted cloudy		Total cases	Predicted clear		Predicted cloudy			
			#	TPR	#	FNR		#	FPR	#	TNR		
Desert	Water	326	212	65%	114	35%	20	0	0%	20	100%	67%	100%
Desert	Ice	329	57	17%	272	83%	21	3	14%	18	86%	21%	95%
Ice	Water	350	350	100%	0	0%	1	1	100%	0	0%	100%	100%
Ice	Ice	366	1	0%	365	100%	28	0	0%	28	100%	7%	100%
Land	Water	1258	845	67%	413	33%	447	9	2%	438	98%	75%	99%
Land	Ice	1213	919	76%	294	24%	419	85	20%	334	80%	77%	92%
Ocean	Water	3447	678	20%	2769	80%	1049	70	7%	979	93%	37%	91%
Ocean	Ice	3299	1879	57%	1420	43%	1112	115	10%	997	90%	65%	94%

## 5 CONCLUSIONS

In this work a hierarchy of neural network committees, trained with increasing amounts of cloud water and ice, were used to predict cloud water ( $c_w$ ) and cloud ice ( $c_i$ ), their effective scattering heights ( $p_{c_w}$  and  $p_{c_i}$ ), respectively) and the column water vapor amount ( $w$ ). The predictions were based on high resolution spectra of reflected sun light in three near-infrared spectral bands (O<sub>2</sub> A-band, weak CO<sub>2</sub> band and strong CO<sub>2</sub> band). This was done in both the nadir and sun-glint viewing modes over all surface types.

Simulated spectra for neural network training were generated from an ensemble of ECMWF profiles containing a large range of atmospheric, cloud and surface types. A principal components analysis was performed on each waveband to compress the data by more than two orders of magnitude and to increase the ability of the algorithm to distinguish information from random clutter.

Sensitivity tests were performed by adding random variations to the predictor values, including the addition of noise to the measurements. Even though the scatter in the retrieval of cloud properties was found to increase due to addition of uncertainties, the ability of the algorithm to classify scenes as either cloudy or clear was only degraded by a few percent.

Testing on an independent data set, generated using CloudSat and Calipso profiles with the uncertainties added, showed favorable classification skill in both viewing modes when using a cloudy-clear threshold of 2 gm<sup>-2</sup> for cloud water and 10 gm<sup>-2</sup> for cloud ice. The classification accuracies vary with the surface type, but are typically in the range 35% to 75%, with positive predictive values (confidence level) typically in the range 80% to 99%. While the predictive skill for cloud properties generally was high for high cloud amounts, below the thresholds the algorithm functioned only as a classifier.

## Acknowledgments

The authors would like to thank Adam Carheden at CSU/CIRA for providing invaluable support with the computer cluster and to Natalie Tourville for her assistance with general computing issues. Thanks also are due to Chris O'Dell and Igor Polonsky for their assistance with various aspects of the radiance simulations. In addition we would like to thank two anonymous reviewers for providing useful suggestions on this work. This research was funded by JPL contracts 1280999 and 1380533.

## References

- [1] T. E. Taylor and D. M. O'Brien, "A neural network cloud screening algorithm. Part I: a synthetic case over land surfaces using micro-windows in O<sub>2</sub> and CO<sub>2</sub> near infrared absorption bands with nadir viewing," *J. Appl. Rem. Sens.* **3**, 033548 (2009) [[doi:10.1117/1.3239515](https://doi.org/10.1117/1.3239515)].
- [2] D. Crisp, C. E. Miller, and P. L. DeCola, "NASA Orbiting Carbon Observatory: measuring the column averaged carbon dioxide mole fraction from space," *J. Appl. Rem. Sens.* **2**, 023508 (2008) [[doi:10.1117/1.2898457](https://doi.org/10.1117/1.2898457)].
- [3] C. E. Miller, D. Crisp, P. L. DeCola, S. C. Olsen, J. T. Randerson, A. M. Michalak, A. Alkhaled, P. Rayner, D. J. Jacob, P. Suntharalingam, D. B. A. Jones, A. S. Denning, M. E. Nicholls, S. C. Doney, S. Pawson, H. Boesch, B. J. Connor, I. Y. Fung, D. O'Brien, R. J. Salawitch, S. P. Sander, B. Sen, P. Tans, G. C. Toon, P. O. Wennberg, S. C. Wofsy, Y. L. Yung, and R. M. Law, "Precision requirements for space-based X<sub>CO<sub>2</sub></sub> data," *J. Geophys. Res.* **112**, D10314 (2007) [[doi:10.1029/2006JD007659](https://doi.org/10.1029/2006JD007659)].
- [4] D. Crisp, R. Atlas, F.-M. Breon, L. R. Brown, J. Burrows, P. Ciais, B. J. Connor, S. C. Doney, I. Y. Fung, D. J. Jacob, C. E. Miller, D. O'Brien, S. Pawson, J. T. Randerson, P. Rayner, R. J. Salawitch, S. P. Sander, B. Sen, G. L. Stephens, P. P. Tans, G. C. Toon, P. O. Wennberg, S. C. Wofsy, Y. L. Yung, Z. Kuang, B. Chudasama, G. Sprague, B. Weiss, R. Pollock, D. Kenyon, and S. Schroll, "The Orbiting Carbon Observatory (OCO) mission," *Adv. Space Res.* **34**, 700–709 (2004) [[doi:10.1016/j.asr.2003.08.062](https://doi.org/10.1016/j.asr.2003.08.062)].
- [5] B. J. Connor, H. Boesch, G. Toon, B. Sen, C. Miller, and D. Crisp, "Orbiting Carbon Observatory: inverse method and prospective error analysis," *J. Geophys. Res.* **113**, D05305 (2008) [[doi:10.1029/2006JD008336](https://doi.org/10.1029/2006JD008336)].
- [6] F.-M. Bréon, D. M. O'Brien, and J. D. Spinhirne, "Scattering layer statistics from space borne GLAS observations," *Geophys. Res. Lett.* **32**, L22802 (2005) [[doi:10.1029/2005GL023825](https://doi.org/10.1029/2005GL023825)].
- [7] F. Chevallier, "Sampled databases of 60-level atmospheric profiles from the ECMWF analyses," SAF Programme Research Report 4, EUMETSAT/ECMWF, Darmstadt, Germany (2001).
- [8] C. Cox and W. H. Munk, "The measurement of the roughness of the sea surface from photographs of the sun's glitter," *J. Opt. Soc. Amer.* **44**, 838–850 (1954) [[doi:10.1364/JOSA.44.000838](https://doi.org/10.1364/JOSA.44.000838)].
- [9] E. C. Monahan and I. ÓMuircheartaigh, "Optimal power-law description of oceanic whitecap coverage dependence on wind speed," *J. Phys. Oceanogr.* **10**, 2094–2099 (1980) [[doi:10.1175/1520-0485\(1980\)010<2094:OPLDOO>2.0.CO;2](https://doi.org/10.1175/1520-0485(1980)010<2094:OPLDOO>2.0.CO;2)].
- [10] D. M. O'Brien, I. Polonsky, P. Stephens, and T. E. Taylor, "Feasibility of cloud screening using proxy photon pathlength distributions derived from high-resolution spectra in the near infrared," *J. Atmos. Oceanic Technol.* **27**, 135–146 (2010) [[doi:10.1175/2009JTECHA1340.1](https://doi.org/10.1175/2009JTECHA1340.1)].
- [11] E. P. Shettle and R. W. Fenn, "Models for the aerosols of the lower atmosphere and the effects of humidity variations on their optical properties," Tech. Rep. Environment. Res., No. 676, AFGL-TR-79-0214, Air Force Geophys. Lab., Hanscom Air Force Base, MA (1979).
- [12] A. K. Heidinger, C. O'Dell, R. Bennartz, and T. Greenwald, "The successive-order-of-interaction radiative transfer model: Part I: model development," *J. Appl. Meteorol. Clim.* **45**, 1388–1402 (2006) [[doi:10.1175/JAM2387.1](https://doi.org/10.1175/JAM2387.1)].
- [13] C. O'Dell, A. K. Heidinger, T. Greenwald, P. Bauer, and R. Bennartz, "The successive-order-of-interaction radiative transfer model: Part II: model performance and applications," *J. Appl. Meteorol. Clim.* **45**, 1403–1413 (2006) [[doi:10.1175/JAM2409.1](https://doi.org/10.1175/JAM2409.1)].

- [14] C. W. O'Dell, "Acceleration of multiple-scattering, hyperspectral radiative transfer calculations via low-streams interpolation," *J. Geophys. Res.* (2010) in press.
- [15] G. H. Golub and C. Reinsch, "Singular value decomposition and least squares solutions," *Numer. Math.* **14**, 403–420 (1970) [[doi:10.1007/BF02163027](https://doi.org/10.1007/BF02163027)].
- [16] S. R. Kawa, D. J. Erickson, S. Pawson, and Z. Zhu, "Global CO<sub>2</sub> transport simulations using meteorological data from the NASA data assimilation system," *J. Geophys. Res.* **109**, 18312 (2004) [[doi:10.1029/2004JD004554](https://doi.org/10.1029/2004JD004554)].
- [17] H. Bösch, G. C. Toon, B. Sen, R. A. Washenfelder, P. O. Wennberg, M. Buchwitz, R. de Beek, J. P. Burrows, D. Crisp, M. Christi, B. J. Connor, V. Natraj, and Y. L. Yung, "Space-based near-infrared CO<sub>2</sub> measurements: testing the Orbiting Carbon Observatory retrieval algorithm and validation concept using SCIAMACHY observations over Park Falls, Wisconsin," *J. Geophys. Res.* **111**, D23302 (2006) [[doi:10.1029/2006JD007080](https://doi.org/10.1029/2006JD007080)].